

Analysis of a Simulated Tropical Cyclone Eyewall Replacement Cycle

JEFFREY D. KEPERT *

Centre for Australian Weather and Climate Research

DAVID S. NOLAN

Rosenthal School of Marine and Atmospheric Science, University of Miami, Miami, Florida

Extended abstract, AMS 31st Conference on Hurricanes and Tropical Meteorology

April 24, 2014

1. Introduction

The fundamental dynamics of the tropical cyclone eyewall replacement cycle (ERC), after the outer eyewall has formed, have been understood for three decades (Shapiro and Willoughby 1982; Willoughby et al. 1982). In contrast, the cause of the initial formation of the outer eyewall has proved to be more elusive. Numerous theories have been proposed (see the reviews by Rozoff et al. 2012; Wu et al. 2012) but a consensus has not been achieved. More recently, attention has focussed on the possible role of the boundary layer in secondary eyewall formation (SEF) (Huang et al. 2012; Kepert 2013; Abarca and Montgomery 2013). Therefore, it is of interest to diagnose the boundary-layer processes occurring during SEF and the subsequent evolution of the eyewalls. This report describes our analysis of a SEF/ERC simulated by a high-resolution WRF simulation of a hurricane.

2. The simulation

Nolan et al. (2013) describe a multiply-nested WRF simulation of a hurricane life-cycle, intended as a “nature run” for data assimilation research. This simulation featured a complete ERC; full details may be found in Nolan et al.

(2013). In this analysis, we use data from the finest mesh, a 1-km grid, output every 6 minutes. These data were azimuthally averaged and interpolated to a uniform height grid. A low-pass time filter with a half-power point of 54 minutes was applied to remove short-term transients. Figure 1c shows a radius-time diagram of the diabatic heating averaged between 1- and 3-km height, showing the initial contraction and intensification of the first eyewall from 0000 to 1800UTC 3 August, the formation of the outer eyewall at about 0000UTC 4 August, and its subsequent contraction and intensification to 0000UTC 5 August. During the intensification and contraction of the outer eyewall, the inner eyewall weakens, then disappears at about 1200 UTC 4 August. Figure 1a shows the corresponding evolution of the gradient wind at 2.2 km height, with the formation of the initial wind maximum and its replacement by the outer being readily apparent. Note also the outwards expansion of the wind field, discussed also by Wu et al. (2012), Huang et al. (2012), Kepert (2013) and Stenger and Elsberry (2014). Figure 1b shows the vorticity of this gradient wind; note that the outwards expansion of the diabatic heating from 1800 UTC 3 August to 0000UTC 4 August and the subsequent inwards contraction of the outer heating maximum are accompanied by a similar evolution of the gradient vorticity.

Figure 2(a,b,c) summarizes the evolution of the boundary layer flow in the simulation

* *Corresponding author address:* Centre for Australian Weather and Climate Research, Bureau of Meteorology, 700 Collins St, Docklands Vic 3008, Australia.
E-mail: J.Kepert@bom.gov.au

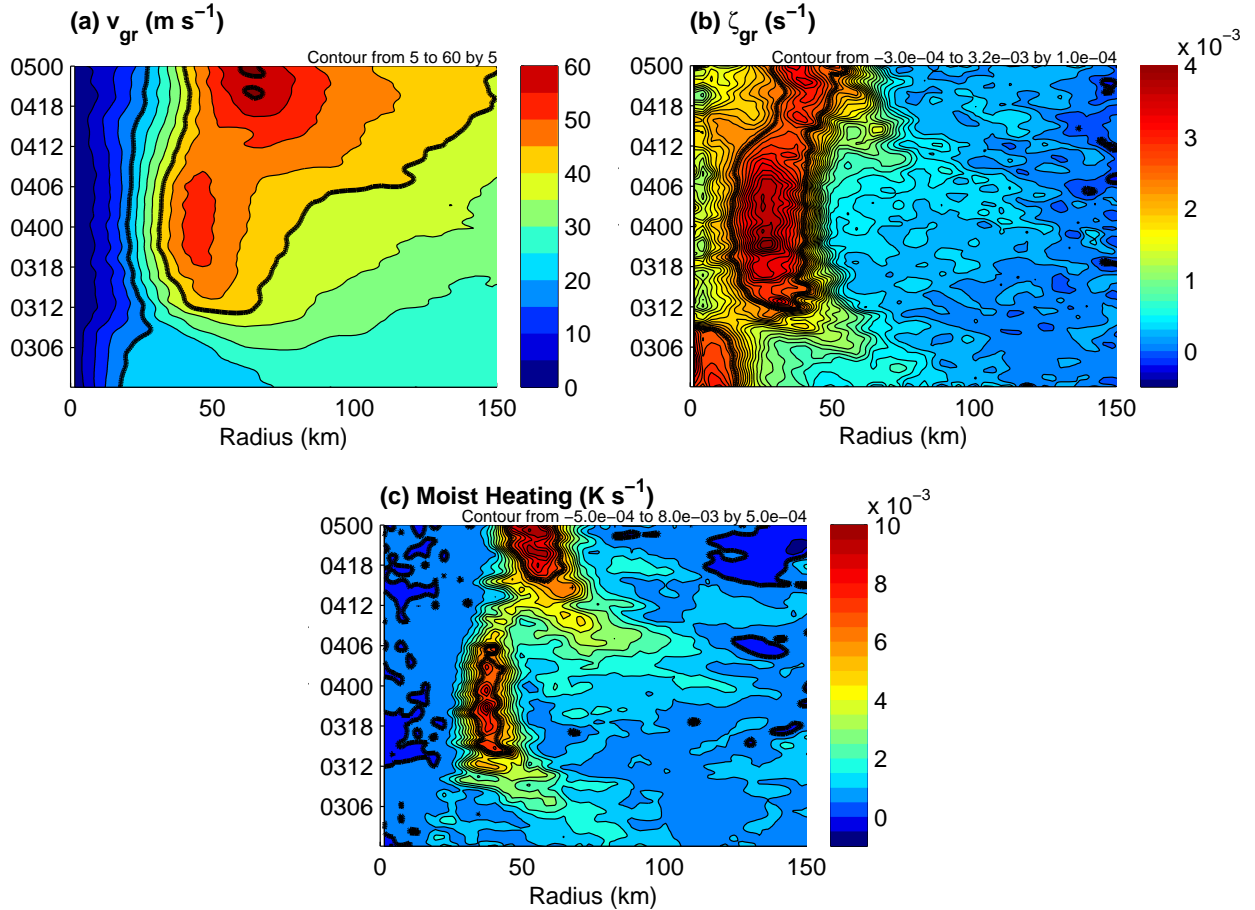


FIG. 1. Hovmöller diagrams from the time-filtered WRF simulation. (a) Gradient wind at 2.2-km height, contour interval $5 m s^{-1}$, thick contour interval $20 m s^{-1}$. (b) Vorticity of the 2.2-km gradient wind, contour interval $10^{-4} s^{-1}$, thick contour interval $2 \times 10^{-3} s^{-1}$. (c) Diabatic heating rate averaged between 1 and 3-km height, contour interval $5 \times 10^{-4} K s^{-1}$, thick contour interval $5 \times 10^{-3} K s^{-1}$.

through the same period. The updraft at 1-km height (Fig. 2c) closely follows the evolution of the diabatic heating. The surface inflow (Fig. 2a) and azimuthal flow (Fig. 2b) display similar maxima and outwards expansion to the gradient wind (Fig. 1a).

3. What are the boundary-layer dynamics?

To understand the contribution of the boundary layer to SEF/ERC, we need to determine the extent to which boundary-layer dynamics (specifically, the effects of surface friction and vertical diffusion) are responsible for the evo-

lution seen in Figs. 1 and 2(a,b,c). Diagnosing cause and effect solely from the output of a full-physics model such as WRF can be difficult because many interacting processes are present. Therefore simplified models are a useful tool, because by eliminating some processes they help isolate the contribution of others, thereby simplifying the interpretation. Here, we use for this purpose two diagnostic models of the tropical cyclone boundary layer, each of which aims to diagnose the boundary layer flow as the steady-state response to an imposed, axisymmetric pressure field that represents the rest of the cyclone. In particular, we use the model of Kepert and Wang (2001) as modified by Kepert (2012), which nu-

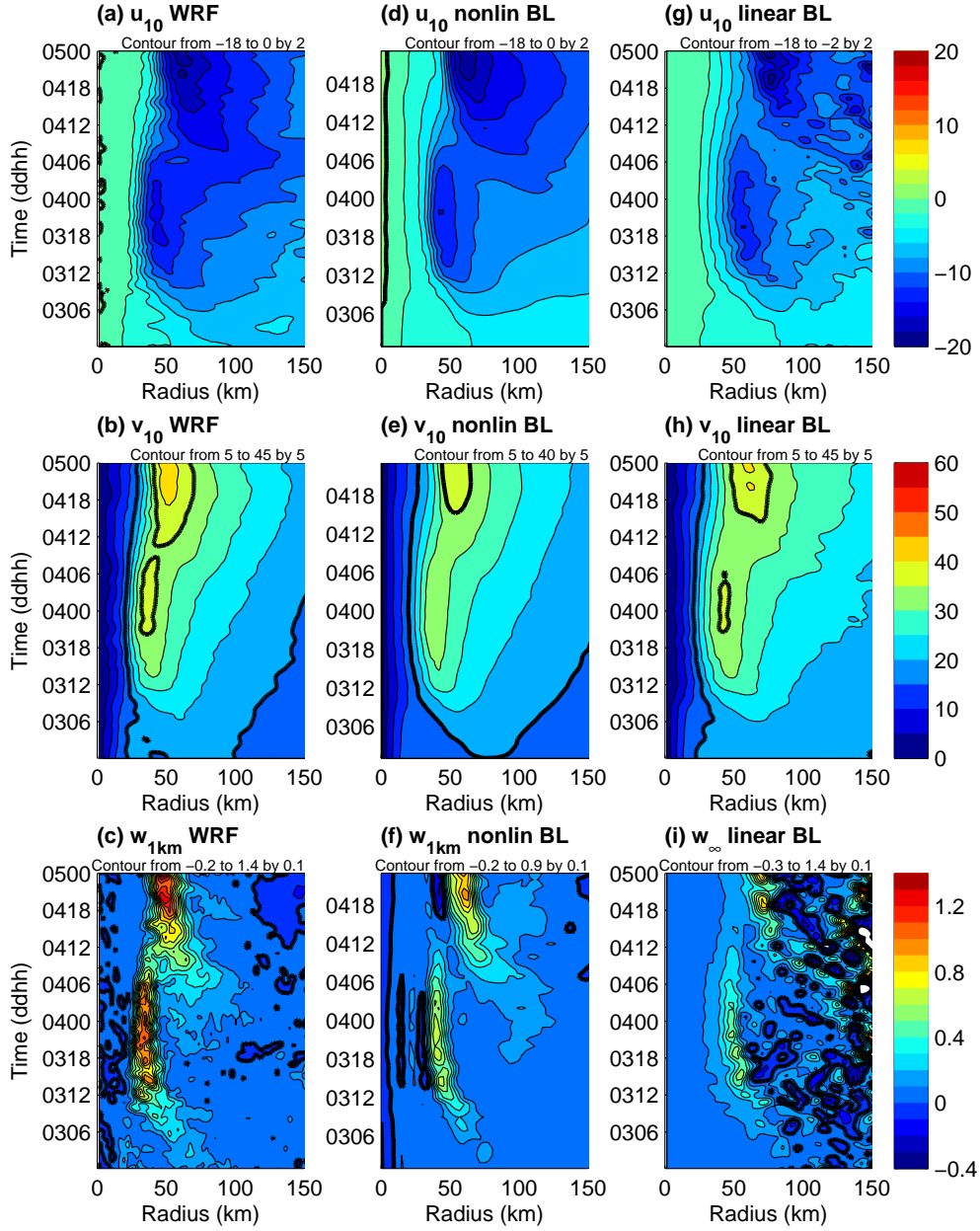


FIG. 2. Hovmöller diagrams of the boundary-layer flow from WRF and two diagnostic models. (a) 10-m radial flow from WRF, contour interval 2 m s^{-1} . (b) 10-m azimuthal flow from WRF, contour interval 5 m s^{-1} . (c) 1-km vertical velocity from WRF, contour interval 0.1 m s^{-1} . (d – f) As for (a – c), except according to the nonlinear boundary-layer model. (g – i) As for (a – c), except according to the linear boundary-layer model.

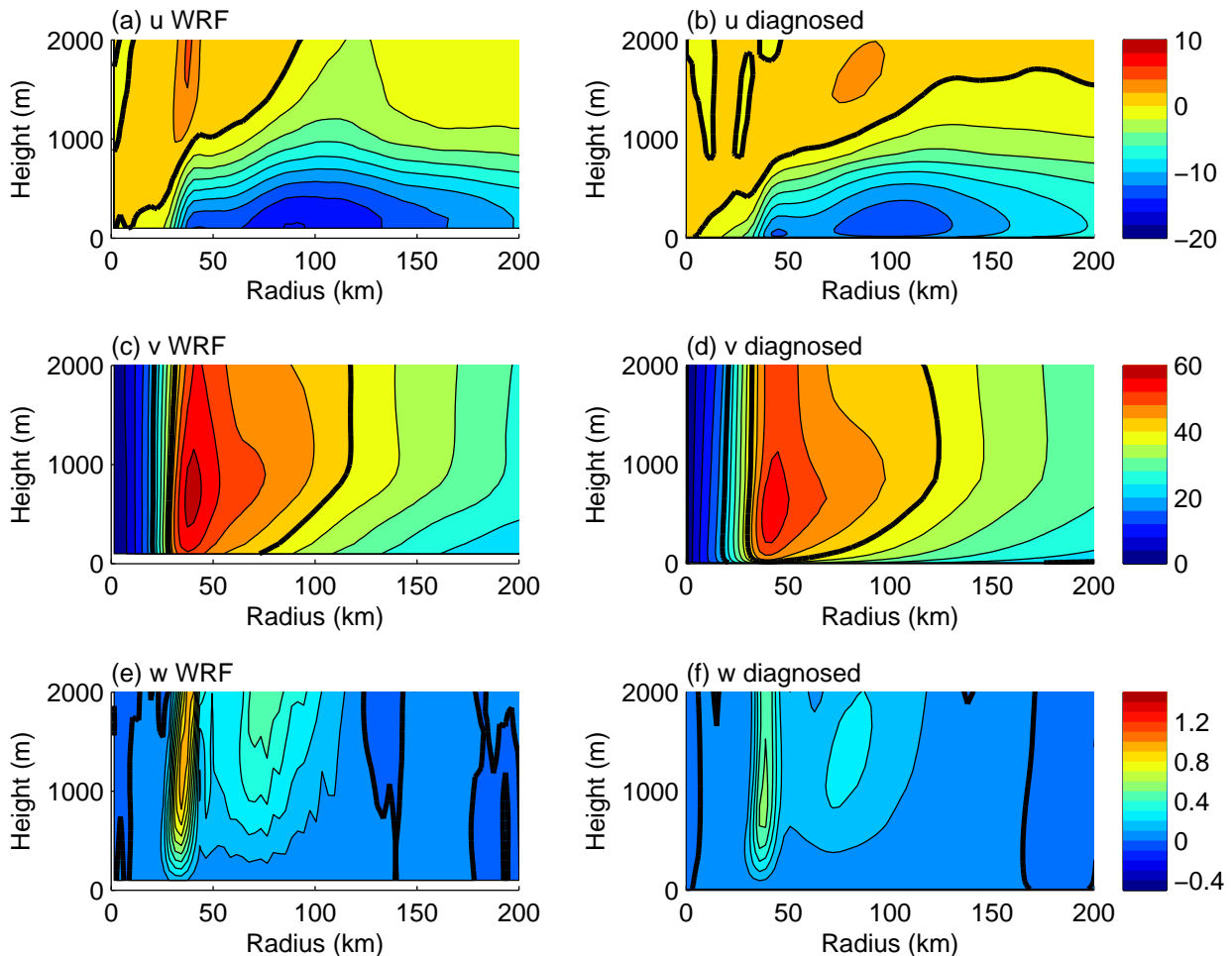


FIG. 3. Radius-height sections of radial, azimuthal and vertical velocity from the WRF simulation at 0600UTC 4 August (left column) and as diagnosed by the nonlinear boundary-layer model (right). Contour intervals are: top row, 2 m s^{-1} , zero heavy; middle row, 4 m s^{-1} , multiples of 20 m s^{-1} heavy; bottom row, 0.1 m s^{-1} , zero shown heavy.

merically solves the full nonlinear version of this problem with realistic physical parameterisations. The physical parameterisations in the nonlinear model were modified as described in Kepert and Nolan (2014) to make them more consistent with those used in the WRF simulation. We also use the linearized boundary-layer model of Kepert (2001), which, by linearizing the problem and using simpler physical parameterisations than the nonlinear model, achieves an analytical solution. This solution is, naturally, less accurate than that from the nonlinear model, but, being analytical, is easier to interpret physically. We shall henceforth refer to these two

models as the nonlinear boundary-layer model and linear boundary-layer model, respectively. Kepert (2013) includes a detailed comparison of these two models in the context of SEF/ERC. For the present purposes, a salient result from that comparison is that the two models diagnose similar frictionally-forced updrafts, with the main difference being that the nonlinear model tends to locate the eyewall peak updraft at somewhat smaller radius than the linear model.

The azimuthal-mean, time-filtered pressure and density data from WRF were used to calculate the gradient wind in the usual way, and this field was supplied to the boundary-layer models

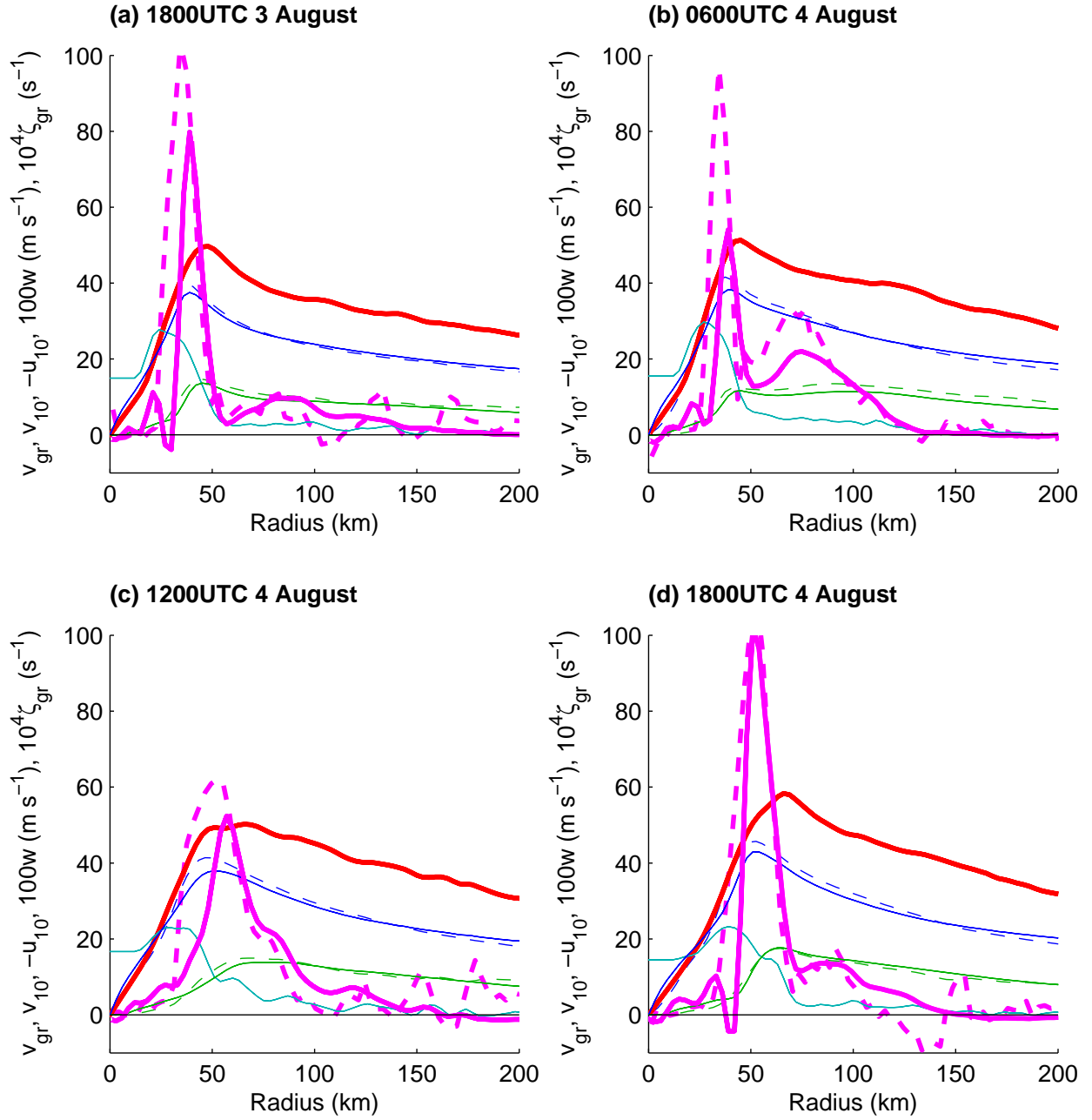


FIG. 4. Comparison of WRF simulation with boundary-layer model diagnosed flow at (a) 1800UTC 3 August, (b) 0600UTC 4 August, (c) 1200UTC 4 August and (d) 1800UTC 4 August. Thick red line: v_{gr} (m s^{-1}), thin cyan line ζ_{gr} (10^{-4}s^{-1}), green lines $-u_{10}$ (m s^{-1}), blue lines v_{10} (m s^{-1}), magenta lines $w_{1 \text{ km}}$ (10^{-2}m s^{-1}). The WRF data is shown as dashed curves, and the boundary-layer model as continuous curves.

at hourly intervals. The boundary-layer models were used to calculate the steady-state flow resulting from each of these forcings. The left-hand panels of Fig. 3 show a radius-height section of the three azimuthally-averaged time-filtered wind components from the WRF simulation at 0600UTC 4 August. At this time, the formation of a secondary wind maximum is under way, although a local azimuthal wind maximum is not yet present. There are two near-surface inflow maxima in the WRF simulation, near $r = 45$ km and $r = 90$ km. These are associated with two updraft maxima, the first near $r = 35$ km, immediately inside of the radius of maximum gradient winds, and a second, broader one near $r = 75$ km. The right-hand panels show the same quantities from a simulation with the nonlinear boundary-layer model forced by the azimuthal-mean pressure gradient force from 2.2-km height in the WRF simulation. The WRF and nonlinear boundary-layer simulations are very similar in structure, but the primary eyewall updraft at its peak is 85% stronger, and the secondary updraft about twice as strong in WRF compared to the nonlinear boundary-layer model. We believe that the main reason for this difference is that the nonlinear boundary-layer model is dry, and therefore the updraft is purely frictionally-forced, while in WRF the updraft is strengthened by the effects of latent heat release (Bui et al. 2009; Rozoff et al. 2012). The boundary-layer inflow and azimuthal flow are both up to 2 m s^{-1} stronger in WRF than in the nonlinear boundary-layer model.

Figure 4 compares the 10-m horizontal flow and 1-km vertical velocity from four times during the ERC (1800 UTC 3 August, and 0600UTC, 1200UTC and 1800UTC 4 August); the second of these times was also shown in Fig. 3. The marked similarities, and relatively small differences, between the WRF and nonlinear boundary-layer model updrafts are similar to those examined in more detail in Fig. 3. This presentation makes another systematic difference clear, in that the 10-m inflow and azimuthal wind components tend to be a little stronger in WRF at most times. The stronger inflow in WRF is consistent, through continuity, with the

stronger updraft there. It is also consistent with the stronger azimuthal winds, since the stronger inflow will advect additional absolute angular momentum inwards, accelerating the azimuthal wind. These differences are expected to be partly due to differences in the vertical mixing between the two models and the effects of azimuthal averaging, but also to the absence of that component of the secondary circulation forced by latent heat release in the boundary-layer model. Nevertheless, it is clear that the diagnostic boundary-layer model reproduces the main features of the boundary-layer flow in the WRF simulation with a high degree of fidelity.

Hovmöller diagrams summarizing the boundary-layer flow evolution from the nonlinear boundary-layer model are presented in Fig. 2(d,e,f). It is clear from a comparison of these to the corresponding plots for WRF (Fig. 2(a,b,c)) that the strong similarity between the WRF and nonlinear boundary-layer simulations applies throughout the 48-hour period studied, and that the systematic differences noted above are representative of those at other times. The only information that the boundary-layer model receives from WRF is the azimuthal-mean pressure gradient force (represented by v_{gr}), which is clearly sufficient for it to reproduce the main features of the boundary-layer flow throughout the simulation, including the vertical velocity. The nonlinear boundary-layer model is equally successful at reconstructing the vertical motion during the initial intensification and eyewall contraction of the storm, during the subsequent formation and contraction of the secondary eyewall, and during the further intensification of the latter eyewall after the primary eyewall has disappeared.

It is also apparent from Fig. 1(a,b) and the red and cyan curves in Fig. 4 that the changes in v_{gr} and ζ_{gr} outside the primary eyewall are quite modest, particularly earlier in the ERC period (from about 1200 UTC 3 August to 0600UTC 4 August). These relatively subtle changes are nevertheless responsible for the marked change in the frictional updraft as the secondary eyewall forms, apparent in the Hovmöller diagram of the simulation with the nonlinear boundary-layer

model from about 1800UTC 3 August (Fig. 2f). The location and timing of this evolution closely matches that in the WRF simulation (Fig. 2c).

We carried out similar computations using the linearized model of Kepert (2001). Our initial results here were similar to those of Xing-Bao Wang (pers. comm. 2012) and Montgomery et al. (2014), in that the vertical velocity was dominated by large-amplitude, short-wavelength fluctuations. The nonlinear model does not produce such oscillations; Kepert and Nolan (2014) argue that the inflowing air passes through the small-scale perturbations in the pressure field that produce the oscillations too quickly to come into equilibrium with the local conditions. The combination of a finite adjustment time and radial advection effectively acts as a low-pass filter of the pressure field. A similar process does not occur in the linear model, as radial advection of the agradient part of the flow has been removed by the linearization. As discussed by Kepert and Nolan (2014), we therefore applied a spatial filter (3 passes of a 1-2-1 filter) to the time-filtered gradient wind field. The results from the linear model applied to time- and space-filtered pressure data are shown in Fig. 2(g,h,i). Inside of about 110-km radius, the solution appears well-behaved and exhibits a narrow updraft near the RMW, and a secondary broader updraft around 90-km radius. Outside of 110-km radius, the solution exhibits large and unphysical oscillations in w , but the linearization here is invalid because the vorticity is low (Kepert 2001, 2013). While some substantial oscillations remain after the spatial filtering, especially at larger radii, the formation and contraction of the successive eyewall updrafts in the linear model is nevertheless discernable through the noise. The systematic displacement of the updraft in the linear model towards larger radius than in the nonlinear boundary-layer model, discussed by Kepert (2013), is also apparent.

4. Discussion

We have seen that the nonlinear boundary-layer model does an excellent job of diagnosing the evolution of the boundary-layer flow in WRF

throughout the whole 48-hour period shown, encompassing the entire SEF/ERC, except that the diagnosed eyewall updrafts are too weak, probably due to the omission of buoyancy. We therefore conclude that frictional convergence within the boundary layer determines the location of the eyewall updrafts in the WRF simulation, and that latent heat release strengthens them. We remind the reader that both boundary-layer models are diagnostic, that is, they calculate the steady flow in response to a fixed axisymmetric pressure field and parameterised surface drag and turbulent mixing.

It is evident from the data shown above, but perhaps most clearly in the four panels of Fig. 4, that quite subtle changes in the pressure field (as displayed there by the gradient wind) can lead to profound changes in the frictional updraft. To better understand those subtle changes, we turn to the linear model and its analytical solution. Kepert (2001) gives an analytical expression for the vertical velocity about the boundary layer in a tropical cyclone according to the linearized model,

$$\begin{aligned} w_\infty &= \frac{1}{r} \frac{\partial}{\partial r} \frac{r C_d v_{\text{gr}} (v_{\text{gr}} + 2v'(0))}{\zeta_{\text{gr}} + f} \\ &= -\frac{1}{(\zeta_{\text{gr}} + f)^2} \frac{\partial \zeta_{\text{gr}}}{\partial r} C_d v_{\text{gr}} (v_{\text{gr}} + 2v'(0)) \quad (1) \\ &\quad + \frac{1}{r(\zeta_{\text{gr}} + f)} \frac{\partial (r C_d v_{\text{gr}} (v_{\text{gr}} + 2v'(0)))}{\partial r}, \end{aligned}$$

This expression was analysed further by Kepert (2013), who showed that the first term on the right-hand side of the expanded version (which he called the vorticity gradient term) dominates over the second (the stress curl term). Figure 5, reproduced from Kepert (2013), plots w_∞ and these two terms for a tropical cyclone with two concentric wind maxima, each of approximately 50 ms^{-1} strength, at radii of 25 km and 75 km. It also shows the vorticity of the gradient wind, from which it is clear that the eyewall updrafts are each collocated with regions of strong radial gradient of ζ_{gr} . The outer wind maximum produces a much stronger updraft than the inner, even though they have similar wind speeds. It is apparent from Fig. 5 that this difference

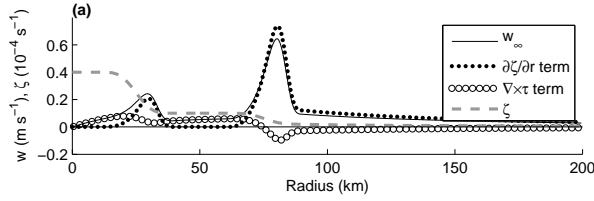


FIG. 5. The vertical velocity according to the linear boundary-layer model (thin black curves) for a case considered by Kepert (2013), and the contributions to the updraft from the vorticity gradient term (dots) and stress curl term (circles) from (1). The vorticity of the parent vortex is shown as the thick grey dashed line. Reproduced from Kepert (2013).

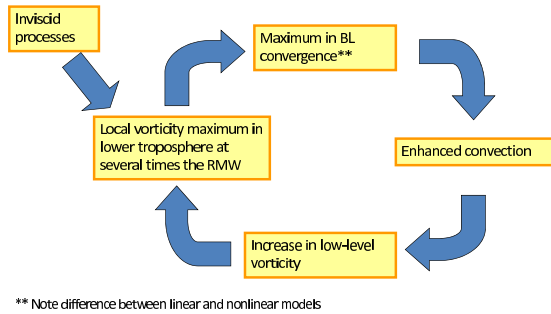


FIG. 6. A schematic diagram of the feedback mechanism proposed by Kepert (2013) for the boundary-layer contribution to secondary eye-wall formation.

is largely due to the vorticity gradient term, and that in this term, the smaller magnitude of $\partial\zeta_{gr}/\partial r$ at the outer wind RMW compared to the inner, is more than compensated by the environment of lower vorticity, as expressed by the factor of $(\zeta_{gr} + f)^{-2}$.

This analysis shows that the distribution of the gradient vorticity is the key to understanding the frictional forcing of the updraft. Indeed, we saw back in Figs. 1 and 2 that there were significant similarities in the evolution of the gradient vorticity, the vertical velocity and the diabatic heating in the WRF simulation. It is now clear that this similarity is no coincidence. The

nonlinear boundary-layer model shows that we may, to good approximation, regard the boundary layer as being “slaved” to the rest of the cyclone, and can accurately diagnose the location and evolution of the eyewall updrafts from the pressure field. The linear model helps to understand the factors that cause these local maxima in frictional convergence, by showing that the gradient vorticity largely determines the frictional updraft. While it tends to place the resulting eyewall updrafts at larger radius than the nonlinear model because it neglects nonlinear advection (Kepert 2013; Kepert and Nolan 2014), this does not alter the fact that the updrafts are largely determined by the gradient vorticity.

The simulation analysed here shows a clear expansion of the wind field prior to and during SEF; similar expansions have also been discussed by others, as noted in the introduction. Kepert (2013) discussed such expansions from the perspective of vorticity changes, and noted that a uniform acceleration of the gradient wind does not produce a local outer maximum in the frictional updraft, but that a nonuniform acceleration could. In particular, the outer updraft was associated with a maximum in the radial gradient of vorticity, and that an acceleration (or equivalently, an expansion of the wind field) which was inhomogeneous, in the sense that the vorticity changes were not uniform in radius, was necessary for the boundary layer to produce a local updraft maximum and thereby become involved in the SEF/ERC. The analysis here, and the Hovmöller diagrams shown in Figs. 1 and 2 strongly support that perspective, with the development of a region of enhanced vorticity gradient and its association with the secondary eye-wall updraft in both WRF and the diagnostic boundary-layer models being apparent.

Based on his analysis of the boundary-layer flow from these two models applied to idealized gradient wind profiles, Kepert (2013) proposed a positive feedback mechanism by which boundary-layer processes contribute to SEF, which is summarised in Fig. 6. It is apparent that the results presented here strongly support this hypothesized feedback loop: in particular that the maxima in the boundary-layer con-

vergence can be diagnosed from the lower tropospheric gradient vorticity (the upper-left arrow of the loop), and that boundary-layer convergence strongly favours convection aloft (the upper-right arrow). Further analysis of this simulation will investigate the remainder of the loop.

Acknowledgments.

D. Nolan was supported in part by the NOAA Office of Weather and Air Quality (OWAQ) through its funding of the OSSE Testbed at the Atlantic Oceanographic and Meteorological Laboratory, by the NOAA Unmanned Aerial Systems (UAS) Program, and by the Hurricane Forecast Improvement Program (HFIP).

REFERENCES

- Abarca, S. F. and M. T. Montgomery, 2013: Essential dynamics of secondary eyewall formation. *J. Atmos. Sci.*, **70**, 3216–3230, doi:10.1175/JAS-D-12-0318.1.
- Bui, H. H., R. K. Smith, M. T. Montgomery, and J. Peng, 2009: Balanced and unbalanced aspects of tropical cyclone intensification. *Quart. J. Roy. Meteor. Soc.*, **135**, 1715–1731, doi:10.1002/qj.502.
- Huang, Y.-H., M. T. Montgomery, and C.-C. Wu, 2012: Concentric eyewall formation in Typhoon Sinlaku (2008). Part II: Axisymmetric dynamical processes. *J. Atmos. Sci.*, **69**, 662 – 674, doi:10.1175/JAS-D-11-0114.1.
- Keper, J. D., 2001: The dynamics of boundary layer jets within the tropical cyclone core. Part I: Linear theory. *J. Atmos. Sci.*, **58**, 2469–2484.
- Keper, J. D., 2012: Choosing a boundary layer parameterisation for tropical cyclone modelling. *Mon. Wea. Rev.*, **140**, 1427–1445, doi:10.1175/MWR-D-11-00217.1.
- Keper, J. D., 2013: How does the boundary layer contribute to eyewall replacement cycles in axisymmetric tropical cyclones? *J. Atmos. Sci.*, **70**, 2808–2830, doi:10.1175/JAS-D-13-046.1.
- Keper, J. D. and D. S. Nolan, 2014: Reply. *J. Atmos. Sci.*, in review.
- Keper, J. D. and Y. Wang, 2001: The dynamics of boundary layer jets within the tropical cyclone core. Part II: Nonlinear enhancement. *J. Atmos. Sci.*, **58**, 2485–2501.
- Montgomery, M. T., S. F. Abarca, R. K. Smith, C.-C. Wu, and Y.-H. Huang, 2014: Comments on "How does the boundary layer contribute to eyewall replacement cycles in axisymmetric tropical cyclones?" by J. D. Keper. *J. Atmos. Sci.*, submitted.
- Nolan, D. S., R. Atlas, K. T. Bhatia, and L. R. Bucci, 2013: Development and validation of a hurricane nature run Using the joint OSSE nature run and the WRF model. *J. Adv. Model. Earth Syst.*, **5**, 1–24, doi:10.1002/jame.20031.
- Rozoff, C. M., D. S. Nolan, J. P. Kossin, F. Zhang, and J. Fang, 2012: The roles of an expanding wind field and inertial stability in tropical cyclone secondary eyewall formation. *J. Atmos. Sci.*, **69**, 583 – 593, doi:10.1002/qj.237.
- Shapiro, L. J. and H. E. Willoughby, 1982: The response of balanced hurricanes to local sources of heat and momentum. *J. Atmos. Sci.*, **39**, 378–394.
- Stenger, R. A. and R. L. Elsberry, 2014: Outer vortex wind structure changes during and following tropical cyclone secondary eyewall formation. *Tropical cyclone research and reviews*, **2**, 196–206.
- Willoughby, H. E., J. A. Clos, and M. G. Shoreibah, 1982: Concentric eyewalls, secondary wind maxima, and the evolution of the hurricane vortex. *J. Atmos. Sci.*, **39**, 395–411.
- Wu, C.-C., Y.-H. Huang, and G.-Y. Lien, 2012: Concentric Eyewall Formation in Typhoon Sinlaku (2008). Part I: Assimilation of T-PARC Data Based on the Ensemble Kalman

Filter (EnKF). *Mon. Wea. Rev.*, **140**, 506 –
527, doi:10.1175/MWR-D-11-00057.1.